An experimental and numerical study on the volume change of particle-filled elastomers in various loading modes

Arne Ilseng[a,b,*], Bjørn H. Skallerud[a], Arild H. Clausen[a]

[a] *Department of Structural Engineering, Norwegian University of Science and Technology, 7491 Trondheim, Norway*
[b] *Aker Solutions AS, 3408 Tranby, Norway*

Abstract

Laboratory tests show that there is a pronounced difference in the volumetric response between uniaxial tension and confined axial compression loading for commercial particle-filled hydrogenated nitrile butadiene rubber (HNBR) and fluoroelastomer (FKM) compounds. In uniaxial tension (UT), a volume increase of 5 and 20 % for the HNBR and FKM respectively was present for a hydrostatic stress of less than 6 MPa, in addition, both compounds showed a clear hysteresis loop in the hydrostatic stress - volume ratio space. For confined axial compression (CAC) tests, on the other hand, the materials reached a 6-7 % volume change for a hydrostatic stress of 140 MPa, and an elastic behaviour was seen. This loading mode dependence of the volumetric response has severe implications for the constitutive representation of the materials. It is demonstrated that existing elastomer models, whereof many assume incompressible volumetric response, are unable to capture the behaviour in both loading modes. To gain an increased understanding of the macroscopically obtained results, a tension in situ scanning electron microscopy study was performed. Matrix-particle debonding was observed to occur at the external surface of the materials, rendering a possible explanation for the loading mode dependent volumetric behaviour. Finite element simulations of a single-particle model, incorporating a cylinder of matrix material with a spherical particle in its centre, showed that the observed debonding can explain the experimental response of the materials in a qualitative manner.

Keywords: Particle-filled elastomers, Volume change, In situ SEM, Single-particle model

1. Introduction

Constitutive models commonly applied to predict the visco-hyperelastic response of elastomers in finite element simulations assume a nearly isochoric behaviour independent of loading mode [1, 2, 3]. Based on available experimental data in uniaxial tension (UT) [4] and confined axial compression (CAC) [5], there are clear indications that this approach can be inaccurate for certain elastomers. It appears that the materials can exhibit a considerable increase of volume in UT,

*arne.ilseng@ntnu.no

while the response in CAC is much stiffer with respect to volume change, yet there is a finite bulk modulus also in this loading case. However, before embarking on the task of developing constitutive models with improved correspondence to experimental observations, an enhanced understanding of the underlying mechanisms causing the loading mode dependent volume behaviour should be provided.

Early work on elastomers (e.g. [6, 7, 8]) mainly dealt with the behaviour of unfilled elastomer gums, for which the assumption of constant volume got accepted as the standard. However, raw gum elastomers have limited industrial application, and filler particles are normally added to the blend of industrial materials [9]. These fillers improve mechanical properties like stiffness and strength, but may also alter the volumetric behaviour of the compounds.

Gent and Park [10] and Cho et al. [11] illustrated the possible effect that stiff particles can have on the volumetric response of elastomers by testing samples of a transparent elastomer matrix with spherical or cylindrical glass inclusions in uniaxial tension. They differentiated the observed response between two failure mechanisms; cavitation, i.e. the occurrence of voids in the material due to stress concentrations near the stiff inclusions; and decohesion, i.e. rupture of the cohesive zone between the inclusion and the matrix material. The failure process was initiated by the occurrence of small voids close to the stiff inclusion, which during deformation grew and coalesced to form larger cavities. As these cavities increased in size, they eventually led to decohesion between the filler particle and the surrounding elastomer matrix. For experiments involving large hydrostatic stresses, Gent and Lindley [12] also found cavitation to occur in unfilled elastomers. This was attributed to pre-existing defects, experiencing unbounded growth when the hydrostatic tension stress exceeded a critical value. Such cavitation under high triaxiality stress states has later been studied further by different authors, e.g. [13, 14, 15]. It is clear that the stress/deformation level where voids would start to grow and the number of voids that would initiate prior to particle decohesion are strongly dependent on properties like the fracture strength of the matrix material, the size and shape of the particles, and the cohesive strength between the matrix and its filler particles. In any event, a process of cavitation and decohesion would lead to a macroscopic volume growth of the material.

For the early research on the volumetric behaviour of elastomers, the most accessible method for measuring global volume changes accompanying deformation was through dilatometry tests [16, 17, 18, 19]. However, the progress of modern measuring techniques has simplified the evaluation of volume changes accompanying deformation significantly through the development of optical methods, like digital image correlation (DIC). Using DIC, Le Cam and Toussaint [20] looked at the competition between volume increase due to void growth and volume decrease due to crystallization in natural rubber loaded in tension. They measured the volume change using DIC at one surface and assuming an isotropic material behaviour. The results showed significantly larger volume growth for particle-filled natural rubber than for unfilled natural rubber. Due to crystallization,

they observed a larger volume during loading compared with unloading. Le Cam and Toussaint [21] also found a significant volume change in filled styrene-butadiene (SBR) dog-bone shaped specimens using a similar set-up. de Crevoisier et al. [22] measured volume growth during cyclic loading of a filled SBR specimen using DIC at two perpendicular surfaces of a dog-bone-shaped specimen. They found the material to behave slightly anisotropic and to display a relatively small volume change. They also reported that the volume change in each deformation cycle started when the longitudinal deformation exceeded the previously obtained maximum deformation. Cantournet et al. [23] recently studied the volume increase of a particle-filled natural rubber under various loading conditions. They measured the volume change occurring under uniaxial tension by use of a video traction system at one surface and the assumption of isotropic material behaviour. The increase in volume was explained by cavitation and decohesion, and this phenomenon was studied using in situ scanning electron microscopy (SEM). They found that for loading at low stress triaxiality, volume growth occurred near ZnO particles, while no debonding could be observed between the elastomer matrix and carbon black particles. For a loading situation of large stress triaxialities, on the other hand, volume growth was seen to be dominated by matrix rupture rather than matrix-particle debonding.

Unit cell simulations are often used to explain globally observed results by studying mechanisms occurring at the scale of the material constituents. Such models have been extensively employed to study ductile fracture in metallic materials, e.g. [24, 25, 26, 27], and to some extent to study the behaviour of particle-filled polymeric materials [28, 29, 30, 31]. Steenbrink et al. [28] and Cheng and Guo [29] looked at the effect of empty voids in glassy polymers by use of axisymmetric cell analyses. Ognedal et al. [30] studied decohesion and volume growth in a mineral-filled PVC using a 3D model to resemble a polymer matrix with spherical particles. For the study of elastomers, Bergström and Boyce [31] looked at how shape, dimension, and stiffness of carbon black particles altered the resulting equilibrium behaviour on the macro scale.

Although the matrix-particle debonding effect in elastomers is experimentally documented in the literature, the implications this have for the macroscopic mechanical response has gained limited attention. In this article, commercial hydrogenated nitrile butadiene rubber (HNBR) and fluoroelastomer (FKM) materials commonly applied for sealing applications in the oil and gas industry are tested in UT and CAC to investigate the difference in volumetric behaviour. To examine the source of the volume growth observed in the UT experiments, an in situ SEM study of tensioned specimens was performed. A single-particle model was then used to see if the behaviour observed in the macroscopic experiments could be explained based on micromechanical effects. No study could be found in the literature neither dealing with the volumetric behaviour of HNBR and FKM elastomers nor debonding or cavitation around particles in such materials. In addition, to the best of the authors' knowledge, single-particle models have not yet been used to study the loading mode dependent volume behaviour of particle-filled elastomeric materials.

The article is organized as follows: The set-up and results for the UT and CAC macroscopic experiments are presented in the following section. Implications of the findings for constitutive modelling of particle-filled elastomers are discussed in Section 3. In Section 4, the set-up and results of the in situ SEM study on the materials are given, while Section 5 studies a single-particle model to explain the macroscopic experimental results in a qualitative manner. In the final section, a summary and some concluding remarks are given.

2. Macroscopic experiments

2.1. Uniaxial tension

2.1.1. Set-up

For the UT tests, one HNBR and one FKM compound commonly used for sealing applications in the oil and gas industry were delivered from two different suppliers as 2 mm thick dog-bone shaped tension specimens with dimensions in line with ISO37 Type 1 and Type 2 respectively [32]. The gauge length of the Type 1 specimens applied for HNBR is 33 mm, while the corresponding length of the Type 2 FKM samples is 25 mm. The specimens were cut from 2 mm thick mats produced by a rolling process. The two materials, their dumbbell geometry, the measured pre-testing density, and the temperature range and hardness values given in the materials data sheets are listed in Table 1. According to the suppliers, the lower bound of the temperature range indicates the temperature for which the materials have fully transitioned into the glassy region.

The specimens were tested using an Instron 5944 testing machine with a 2 kN load cell. The deformation cycle addressed herein exposed the test samples to a maximum machine displacement of 40 mm followed by an immediate unloading until zero force was measured by the load cell. A deformation rate of 1 mm/s was used during both loading and unloading which corresponds to a nominal strain rate of 0.03 s^{-1} for the HNBR material and 0.04 s^{-1} for the FKM.

Table 1: Tested materials, their geometries and properties

Material	Geometry	Density	Temperature range	Hardness
HNBR	ISO 37 - Type 1	1.29 g/cm^3	-35 to 150 °C	86 shore A
FKM	ISO 37 - Type 2	1.77 g/cm^3	-40 to 200 °C	89 IRHD

While the force level F was measured by the load cell of the machine, optical means were used to determine the local deformations in the gauge section. For this purpose, a grey scale speckle pattern was applied to the specimens prior to testing, and two Prosilica GC2450 CCD cameras were used to capture frames of the wide and narrow surface of the specimen throughout the tests. The obtained images were post-processed using the in-house DIC software *eCorr* [33]. An illustration of the tension test sample and the boundaries monitored by the two cameras can be seen in Figure 1. Two repetitions were performed for each material, with the duplicate tests echoing the results presented here.

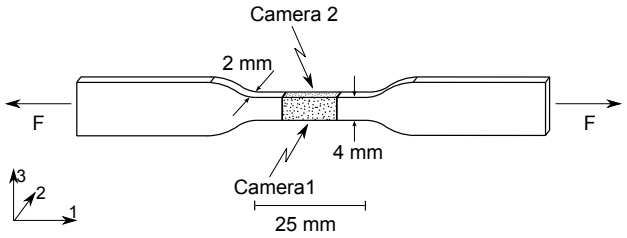

Figure 1: Illustration of the experimental set-up used in the UT experiments, geometrical measures in line with ISO 37 Type 2 used for the FKM samples.

Applying the two perpendicular cameras for the DIC measurements, all three stretch components λ_i, $i = 1,2,3$ with the directions being defined through the Cartesian coordinate system in Figure 1, were obtained throughout the test. Thereby, the volume ratio J was found without using the assumption of material isotropy ($\lambda_2 = \lambda_3$), with J being calculated from

$$J = \frac{V}{V_0} = \lambda_1 \lambda_2 \lambda_3 \tag{1}$$

where V is the current volume and V_0 the reference volume. Further, the logarithmic strain components are found as $\epsilon_i = \ln(\lambda_i)$. In addition, the longitudinal Cauchy stress σ_1 was found in a correct manner, i.e. without using assumptions of isotropic or isochoric ($\lambda_2 = \lambda_3 = 1/\sqrt{\lambda_1}$) material behaviour, through

$$\sigma_1 = \frac{F}{\lambda_2 \lambda_3 A_0} \tag{2}$$

where A_0 is the initial cross sectional area of the specimen. For UT loading, where $\sigma_2 = \sigma_3 = 0$, the hydrostatic stress is defined as

$$\sigma_{vol} = \frac{\sigma_1}{3} \tag{3}$$

The importance of the dual camera set-up is illustrated in Figure 2, showing the longitudinal (positive) and transverse (negative) logarithmic strains obtained by the two cameras for both materials. It is seen that the relative difference between the longitudinal strains measured from the two independent yet synchronized cameras is negligible throughout the tests. For the transverse strains, on the other hand, there is a clear discrepancy caused by transverse anisotropic material behaviour. This transverse anisotropy is assumed to originate in the rolling process used to produce the 2 mm thick sheets from which the specimens were cut. The implications of neglecting this transverse anisotropy when calculating the stress and volume growth during the test are discussed in Section 2.1.2.

2.1.2. Results

The results obtained for the deformation cycle are presented in Figure 3. From the Cauchy stress - logarithmic strain curves displayed in Figure 3a, the initial tension behaviour is seen to be similar for the two materials, while the HNBR compound displays a higher stress level as the strain exceeds 0.2. The FKM sample reaches a larger maximum strain level due to the difference

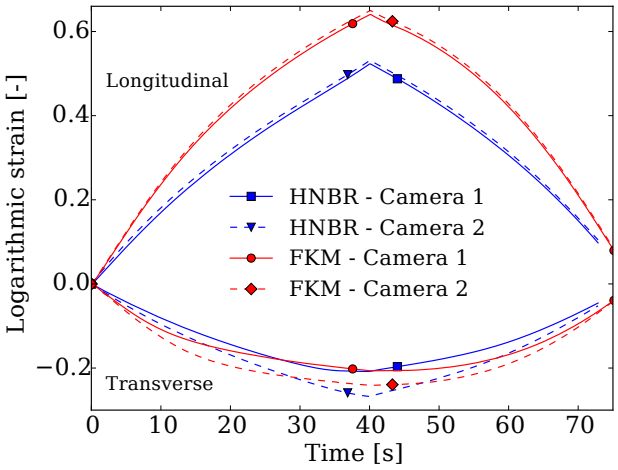

Figure 2: Longitudinal (positive) and transverse (negative) strains calculated by DIC for HNBR and FKM subjected to one deformation cycle in tension.

in initial geometry. The volume ratio for the two materials with respect to longitudinal strain is addressed in Figure 3b. For both materials, the volume ratio is seen to stay close to unity during the first phase of the deformation process, until a critical strain level is reached at which a clear increase in volume ratio begins. The strain level at the onset of volume increase is clearly smaller for the FKM material compared with the HNBR compound. In addition, the maximum volume increase is more than 20 % for the FKM material, opposed to approximately 5 % for the HNBR compound. No study could be found in the literature reporting such a large volume increase at the given strain level for an elastomer as the one found for the FKM material.

In Figure 3c, the hydrostatic stress level is plotted towards the volume ratio. A critical hydrostatic stress (corresponding to the critical strain level) is seen to be required before the volume increase sets on, with a clearly higher stress being needed in the HNBR material compared with the FKM compound.

It should be noted that due to the volume increase, using an assumption of isochoric material behaviour and calculating the stress-strain data using the longitudinal strains from Camera 1 would over-predict the stress level at maximum deformation with about 3 % for the HNBR material and more than 20 % for the FKM material. In addition, due to the transverse anisotropic behaviour of the materials, using data only from Camera 1 and assuming isotropic material behaviour would lead to an over-prediction of the maximum volume change for the HNBR material by 130 %, and a 20 % over-prediction of the volume increase in the FKM compound. The level of material anisotropy in elastomeric tension samples is seldom measured and reported in the literature, and experimental set-ups are often based on an assumption of transverse isotropic material behaviour. Thus, this brief discussion emphasizes the bias a single camera set-up might cause for certain materials.

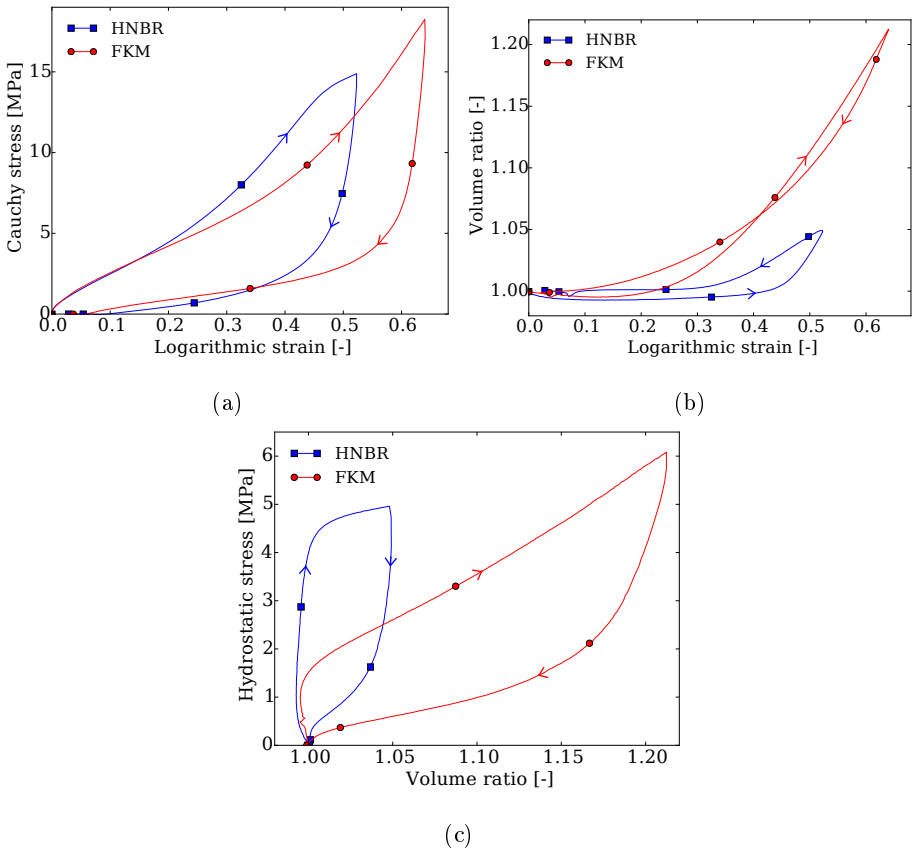

Figure 3: Results from UT experiments (a) stress-strain, (b) volume ratio - logarithmic strain, and (c) hydrostatic stress - volume ratio behaviour. Arrows indicate loading and unloading directions.

2.2. Confined axial compression

2.2.1. Set-up

To evaluate the volumetric response of the samples in nearly hydrostatic compression, a CAC rig was built. A thorough presentation of the set-up was provided by Ilseng et al. [5], however, a brief discussion is included here for completeness. The specimens used for CAC were cylinders with a height of 12.5 mm and a diameter of 29.0 mm (in accordance with ISO 815-1 Type A [34]). While the same HNBR compound could be delivered as samples for both UT and CAC experiments, it was not possible for the supplier to provide a compression specimen of the FKM compound that was tested in tension. However, two other FKM compounds, named FKM1 and FKM2, were delivered with the geometries used for CAC. It is believed that the two other compounds would give an indication of the CAC behaviour of the FKM compound tested in tension.

An illustration of the CAC rig is presented in Figure 4. The rig was designed to be used with an Instron 5982 universal testing machine with a t-slot table, and involves two pistons with load cells and a 20 mm thick steel plate supported on four M16 bolts. The centre hole of the steel plate was produced with a diameter of 29.0 mm and with a tolerance of $+0.05$ mm -0.00 mm, while the two pistons were produced with a diameter of 29.0 mm and a tolerance of $+0.00$ mm

-0.05 mm to ensure a tight fit. The plate was fixed to the t-slot table in the machine by the four steel bolts, while the two pistons were screwed onto the respective load cells. In addition to the 100 kN load cell in the testing machine, an HBM U2A 100 kN load cell was included below the specimen and fixed to the t-slot table with bolts. The purpose of the second load cell was to facilitate measurement of the frictional forces that arise during testing. To avoid dealing with the compliance of the testing machine, a checkerboard pattern was applied to the upper piston and a camera was used to log images of this pattern throughout the tests. By use of a point tracker routine [35], the displacement of the upper piston could be calculated. It was assumed that the test set-up, which was made of steel, was fully rigid and that all deformation therefore occurred in the specimen. Following Equation 1, this assumption means that the volume ratio can be defined as

$$J = \frac{H}{H_0} \tag{4}$$

where H is the current height of the specimen, while H_0 is the initial height. A silicon grease was applied to all surfaces of the specimens prior to testing, and this treatment was found to reduce the frictional forces between the specimen and the steel plate significantly. Using the grease, the frictional force was less than 1.3 % of the load in the upper load cell at maximum load for all tests.

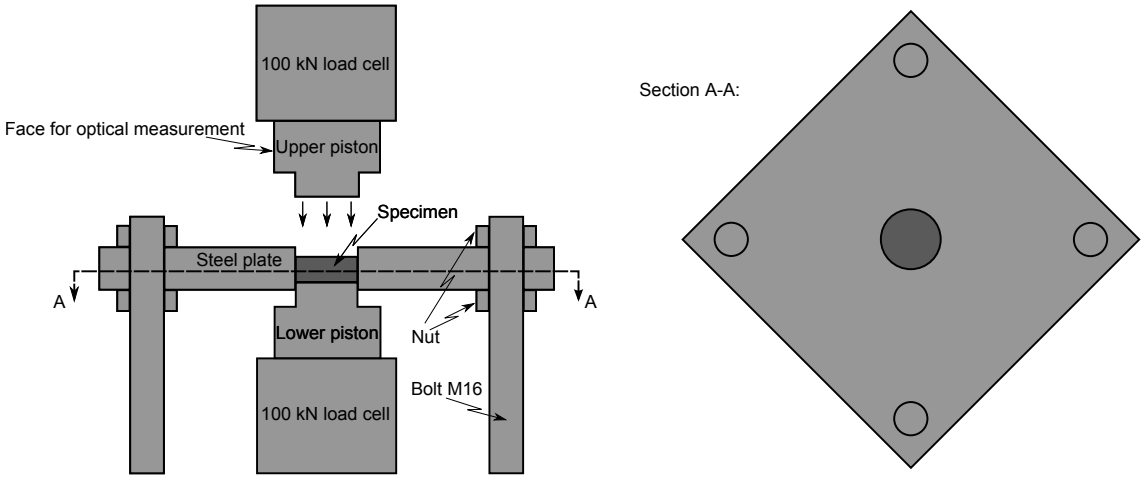

Figure 4: Illustration of the experimental set-up used for the confined axial compression experiments.

All specimens were tested by a cyclic loading history, obtaining a force in the upper load cell of 95 kN before returning to 0.1 kN and starting a new cycle. A deformation rate of 3 mm/min was applied during both loading and unloading. In the sixth cycle, the load level was kept constant at 95 kN for 30 minutes as a volumetric creep test.

Denoting the force measured in the upper load cell by F and the area of the circular cross section of the specimen as A_0, the axial stress in the specimen can be found by the relation

$$\sigma_{zz} = \frac{F}{A_0} \tag{5}$$

and the corresponding hydrostatic stress level in the material can be found through

$$\sigma_{vol} = \frac{1}{3}\left(\sigma_{zz} + \sigma_{rr} + \sigma_{\theta\theta}\right) \tag{6}$$

The value of the radial and hoop stress components σ_{rr} and $\sigma_{\theta\theta}$ is not measured in the experimental set-up and would strongly depend on the material behaviour. However, assuming that the tested materials obey the generalized Hooke's law, the three stress components σ_{zz}, σ_{rr}, and $\sigma_{\theta\theta}$ can be calculated as:

$$\sigma_{zz} = \frac{E}{1-2\nu}\frac{1-\nu}{1+\nu}\left(J-1\right) \tag{7}$$

$$\sigma_{rr} = \sigma_{\theta\theta} = \frac{E}{1-2\nu}\frac{\nu}{1+\nu}\left(J-1\right) \tag{8}$$

where the relation for the axial strain reads $\epsilon_{zz} = J - 1$ as $\epsilon_{rr} = \epsilon_{\theta\theta} = 0$. Combining Equation 7 and 8, the stress components σ_{rr} and $\sigma_{\theta\theta}$ can be related to the measured component σ_{zz} through

$$\sigma_{rr} = \sigma_{\theta\theta} = \frac{\nu}{1-\nu}\sigma_{zz} \tag{9}$$

which means that the hydrostatic stress level can be calculated as $\sigma_{vol} = \frac{1+\nu}{3(1-\nu)}\sigma_{zz}$. The relation between the hydrostatic stress in the specimen and the axial stress measured in the experiment is then a function of the Poisson's ratio of the tested material as

$$\frac{\sigma_{vol}}{\sigma_{zz}} = \frac{1+\nu}{3\left(1-\nu\right)} \tag{10}$$

This relation between the hydrostatic stress in the specimen and the measured axial stress is shown for a Poisson's ratio between 0 and 0.5 in the plot of Figure 5. Clearly, the measured axial stress presents an upper bound for the hydrostatic stress level in the specimen, however, the error is limited for materials with a Poisson's ratio close to 0.5. As a Poisson's ratio of more than 0.49 was measured for both materials at a longitudinal logarithmic strain of 0.1 (i.e. before any significant volume increase) in the UT tests of Section 2.1, the set-up is thought to yield valuable data for the purpose of the present study. A further discussion on the relation between the measured axial stress and the actual hydrostatic stress for the tested materials is given in Section 2.2.2.

2.2.2. Results

The raw force-displacement data obtained for the six loading cycles on the HNBR material is presented in Figure 6a. Qualitatively, this response is also representative for the two FKM materials. It can be seen that the force level is nearly zero the first 0.4 mm of deformation. This is interpreted as the deformation needed to obtain full contact between the two pistons and the specimen. Thereafter, the stiffness is gradually increasing until a constant level is reached at approximately 0.6 mm of deformation. This stage is interpreted as mainly deviatoric deformation needed to obtain full contact between the specimen boundaries and the hole in the steel plate. For the rest of the loading and the following cycles, a nearly constant stiffness and no significant hysteresis or cycle dependence can be seen. For the creep test, only a slight volume increase can

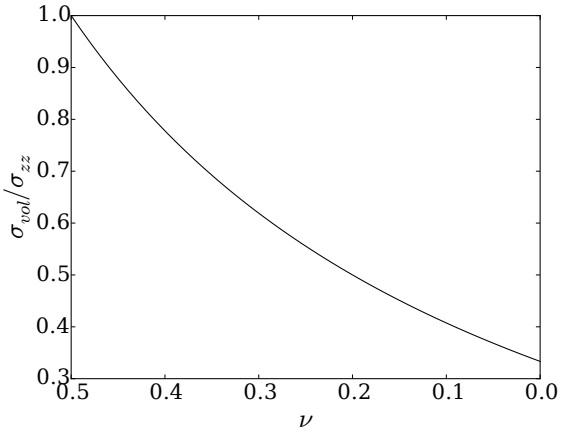

Figure 5: The relation between the hydrostatic and axial stress for different levels of the Poisson's ratio ν.

be observed. As the deviatoric behaviour of the material has been found to be viscous and cycle dependent [4] the deformation in this stage is likely to be dominated by the hydrostatic stresses, meaning that the measured axial stress defined in Equation 5 yields a good approximation to the hydrostatic stress response of the tested materials. In the following results, the measured axial stress is therefore denoted as the hydrostatic stress.

The hydrostatic stress - volume ratio behaviour obtained during loading in the fifth deformation cycle for the three materials can be seen in Figure 6b. A relatively similar response is seen for the HNBR and the FKM1 materials with 6 % volume increase at a hydrostatic stress of 140 MPa, while the FKM2 material shows a slightly more compliant volumetric response with 7 % volume increase at maximum stress.

It should be noted that the volumetric response obtained in CAC differs significantly from that obtained in UT, see Figure 3c, where a volume increase of respectively 5 and 20 % was achieved for a hydrostatic stress of less than 6 MPa. Some implications of this loading mode dependent volume behaviour for the constitutive modelling of particle-filled elastomers are discussed in the following section.

3. Implications for constitutive modelling

In constitutive modelling of elastomeric materials, it is common to split a hyperelastic strain energy potential W additively in an isochoric and a volumetric contribution

$$W = W_{iso}\left(I_1^*, I_2^*\right) + W_{vol}\left(J\right) \tag{11}$$

where I_1^* and I_2^* are the first and second invariant of the distortional left Cauchy-Green deformation tensor, while J still defines the volume ratio of the material. From this potential function, the hydrostatic stress term can be found as

$$\boldsymbol{\sigma}_{vol} = \frac{\partial W_{vol}}{\partial J}\mathbf{I} = \sigma_H \mathbf{I} \tag{12}$$

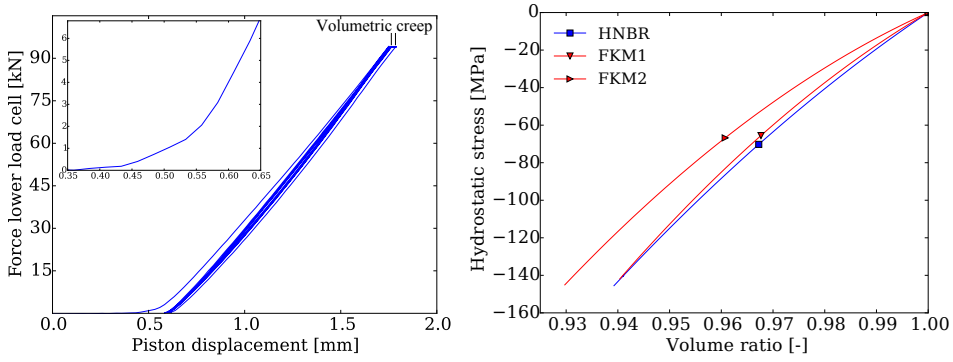

(a) (b)

Figure 6: Results from confined axial compression experiments. (a) Force - displacement data for the HNBR material subjected to six loading cycles, the inset illustrates the force increase from 0.35 to 0.65 mm of piston displacement in the first loading cycle and (b) hydrostatic stress - volume ratio behaviour obtained during loading in the fifth deformation cycle for all three compounds.

While a wide range of both phenomenological and physically based functional forms for the isochoric response has been proposed and discussed in the literature [36], the number of functional forms for the volumetric behaviour is limited. Different phenomenological volumetric hyperelastic potential functions were discussed by Doll and Schweizerhof [37] and by Bischoff et al. [38], and three of the more commonly applied forms for the volumetric part are [39, 40, 41]

$$\begin{aligned} W^a_{vol} &= \frac{\kappa}{2}\left(J-1\right)^2 \Rightarrow \sigma^a_H = \kappa\left(J-1\right) \\ W^b_{vol} &= \frac{\kappa}{2}\left(\frac{J^2-1}{2} - \ln J\right) \Rightarrow \sigma^b_H = \frac{\kappa}{2}\left(J - \frac{1}{J}\right) \\ W^c_{vol} &= \frac{\kappa}{2}\left(\ln J\right)^2 \Rightarrow \sigma^c_H = \kappa\left(\frac{\ln J}{J}\right) \end{aligned} \tag{13}$$

In Figure 7, the parameter κ of the three different volumetric terms given in Equation 13 is optimized to fit the CAC data for the FKM1 material. The predicted hydrostatic stresses companying a volume increase are then compared with the volumetric data obtained for the FKM material in the UT experiment. While it is seen that all three expressions for the volumetric part of the strain energy potential yield a good correspondence with the CAC data, none of them are capable of predicting the compliant volumetric response in UT.

In addition to the large difference in volumetric response between UT and CAC, purely hyperelastic material models would not be able to capture the hysteresis loop in hydrostatic stress - volume ratio space seen in Figure 3c. While Reese and Govindjee [42] introduced a constitutive framework for viscous volume growth, most models aiming to predict the viscoelastic response of elastomeric materials assume a nearly isochoric behaviour, and only stiff and elastic volumetric deformations are included [1, 2, 3].

Clearly, a new modelling approach is needed to capture the behaviour seen in the macroscopic experiments. An important feature of such a model would be the ability to predict a compliant

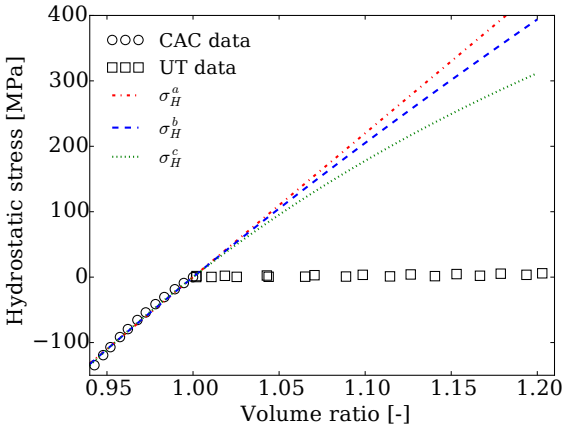

Figure 7: Comparison of different hydrostatic stress terms proposed in literature with experimental data for FKM in UT and CAC.

viscous volume growth for loading modes including positive hydrostatic stresses, at the same time as a stiff and elastic volume response would be predicted in hydrostatic compression. To the best of the authors' knowledge, none of the constitutive models in the literature aimed at modelling elastomeric behaviour includes these effects. However, before one embarks at the task of deriving new constitutive equations, more knowledge on the mechanisms causing the observed macroscopic behaviour should be obtained. Therefore, the rest of this paper is devoted to study the observed response in more detail, while the derivation of a new model is postponed to a forthcoming paper.

The significant difference in volume change between the two loading modes can possibly be explained by cavitation and decohesion occurring near stiff inclusions in UT, while this would not be applicable during CAC deformation. To investigate this hypothesis further, an in situ SEM study is presented in the following section.

4. SEM study

4.1. Set-up

The SEM study was performed using a Zeiss Gemini Ultra 55 Limited Edition microscope at the Department of Materials Science and Engineering, NTNU. This instrument provided micrographs with a resolution of 3072×2072 pixels. A purpose-built tension rig [43] was placed on the sample board of the microscope to enable in situ measurements during uniaxial tension. A photo of the tension rig is shown in Figure 8a. Small tension specimens, having dimensions in line with the sketch in Figure 8b, were cut from the ISO geometry tension specimens delivered by the suppliers, i.e. cut from untested samples from the same production batch of specimens as those tested in macroscopic uniaxial tension.

Prior to any deformation, images at 60, 100 and 300 times magnification were obtained of the surface at both the centre and the edge of the specimen, resulting in six images for each compound. The locations of the pre-deformation images are illustrated in Figure 9, showing an overview image

of the 3 mm wide gauge section surface. These micrographs were analysed using the Python image processing package scikit-image [44] to obtain an indication of the size, number, and distribution of particles at the materials surface. The particles were distinguished from the matrix material by image segmentation, using Otsu's method [45] to define the threshold value, i.e. minimizing the grey-level variance of each segment.

After tensioning the specimens at a nominal strain rate of 0.01 s^{-1} until a nominal longitudinal stretch of 2 was reached, the samples were studied again with SEM to look for effects that could explain the macroscopic behaviour seen in Section 2. The samples were then scanned by a random walk procedure and micrographs were captured at sites of interest.

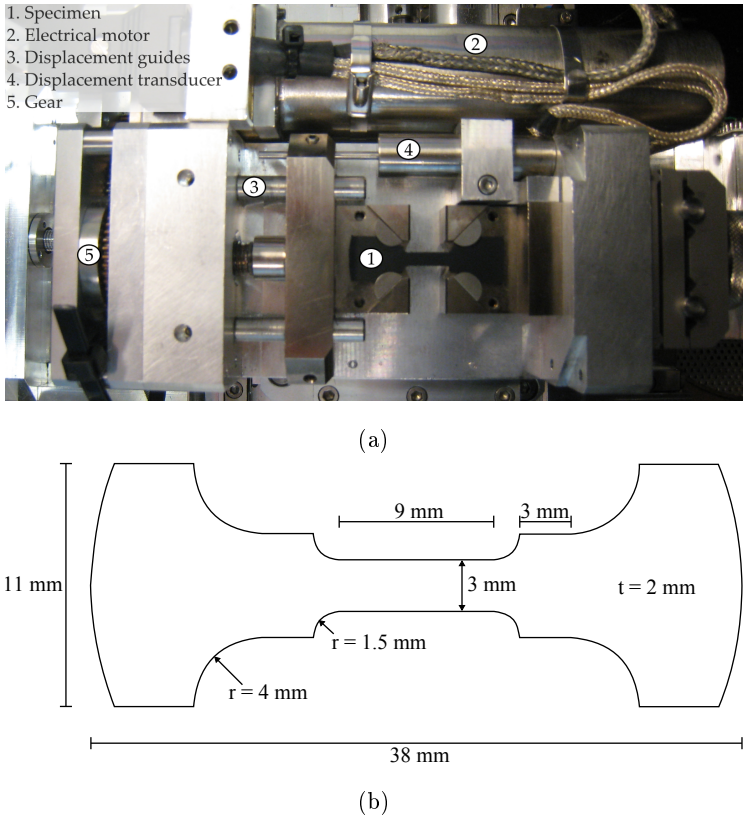

Figure 8: Setup for in situ SEM study. (a) HNBR specimen in tension rig and (b) geometry of specimens cut from virgin ISO dimension tension samples.

4.2. Results

4.2.1. Particle distribution

The pre-deformation micrograph obtained at 60× magnification in the centre of the specimen surface is shown for both materials in Figure 10. A number of highly reflecting inclusions can be seen at the surfaces at this length scale. Energy-dispersive X-ray spectroscopy (EDS) suggested that these, for both the HNBR and the FKM material, are ZnO particles. Other filler particles, like carbon black, were not visible at the studied length scale. The geometry of the observed

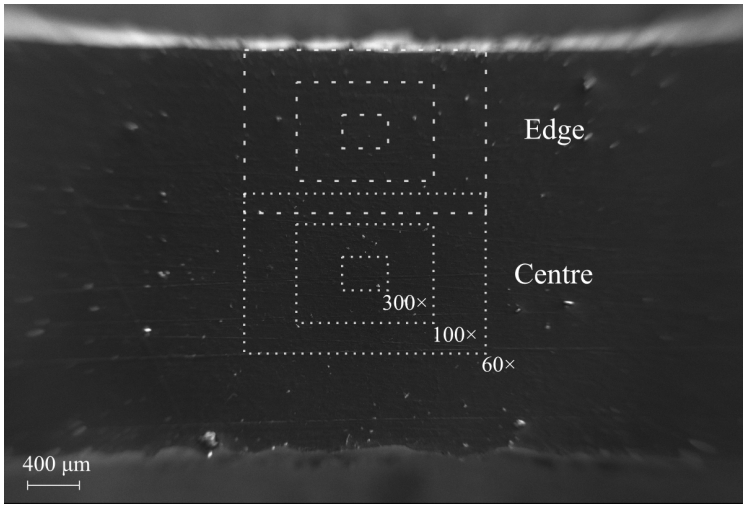

Figure 9: Overview of SEM images of the surface obtained prior to deformation, shown on a micrograph of the HNBR material. The image shows a part of the 9 mm long, 3 mm wide gauge section of the specimens.

particles ranges from nearly circular to oblong shapes, while the particles can be seen to be evenly distributed in the surface without any clear clustering. Dimples can be seen at the surface of the FKM material, but it is not clear if these are representative for voids in the bulk material or only surface effects caused by particles removed from the surface during or after the processing of the samples. However, the fraction of internal voids is expected to be limited, due to the stiff and elastic volume response observed in the CAC experiments. Surface dimples were also observed in images of the HNBR material, although not present in the 60× magnification image from the centre part of the sample shown in Figure 10.

From the segmentation process performed on all pre-deformation images, the total number and size of individual particles could be estimated. The obtained area fraction of particles as function of the applied magnification is plotted for all micrographs in Figure 11a, while the total number of particles is shown in Figure 11b. It is clear that the FKM material contains both a larger area fraction and a larger number of particles at the surface. It should be noted that since the number of particles found at the centre location of the FKM material grows as the magnification increases, the area fraction at the low magnification levels for this material is underestimated, since a subset of the image is found to contain more particles than what were counted in the entire micrograph at 60 and 100 times magnification.

In Figure 11c, the particles identified in the 60× magnification images were numbered according to the size of their projected area. This gives an indication of the distribution between large and small particles. For both materials, the edge of the specimen is seen to contain more and larger particles compared with the centre. It is also clear that the materials contain a high number of small particles, and only a few particles having larger size. The largest particle found in the inspected regions had a projected area of 1125 μm^2, found at the edge of the FKM material, while the smallest particle possible to identify with this method at 60× magnification had a projected

area of 0.09 μm^2.

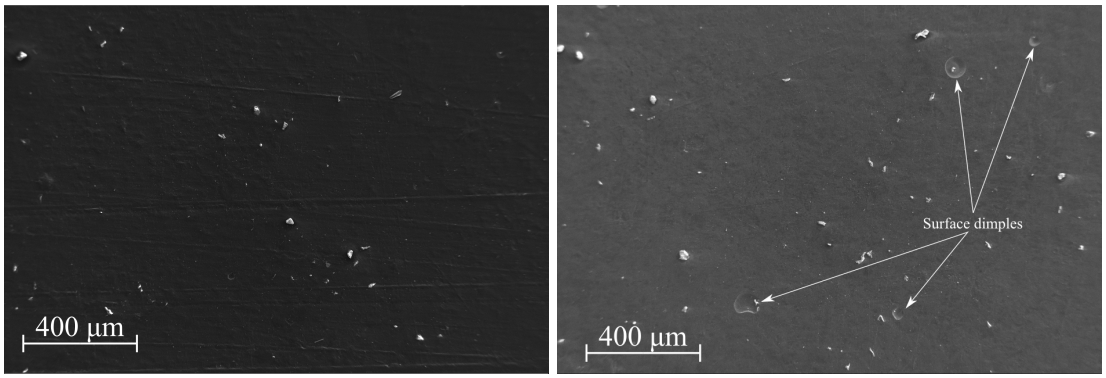

(a) (b)

Figure 10: Pre-deformation SEM images from sample centre at 60× magnification for (a) HNBR and (b) FKM.

4.2.2. Debonding and cavitation

For the in situ tension images, it was found that deforming the specimens changed the conductive properties of the compounds, reducing the image quality at large deformations. This was particularly challenging for the FKM material, yet, matrix-particle debonding and cavitation could be found at the surface of both compounds as illustrated in Figure 12, where sub-figures (a) to (c) address the HNBR material, while (d) addresses the FKM compound.

The image in Figure 12a shows clear debonding at location 1, with cavities formed at both sides of the large particle while the bonding with the matrix seems to be intact at the upper and lower surfaces. At location 2, a cavity is seen with a circular particle near its centre. However, with the cavity being very large compared to the particle, and the particle being completely debonded from the matrix, it is unclear if the cavity is caused by this centre particle or if it is a matrix cavity in the surface caused by the stress situation that incidentally has a centre particle. The particle at location 3 can be seen to have an early-stage debonding at both sides. A slightly different debonding mechanism is illustrated in Figure 12b, where a large crater caused by debonding is seen at location 1, while only slight debonding has taken place at location 2. This one-sided debonding mechanism was also observed for other irregularly shaped particles. Another example is provided in Figure 12c, where the large particle has debonded along the surface at location 1 only. At location 2, on the other hand, matrix cavitation, without any visible interior particle, has taken place in front of the large particle. It should be noted that for the micrographs of the HNBR material in Figure 12, particles fully preserving their bonding to the matrix material could also be observed.

For the FKM compound, one micrograph showing a particle in a large cavity could be obtained, as shown in Figure 12d. Due to the large size of the cavity compared with the particle, it is unclear if the debonding is due to the stress situation caused by the centre particle or due to surrounding

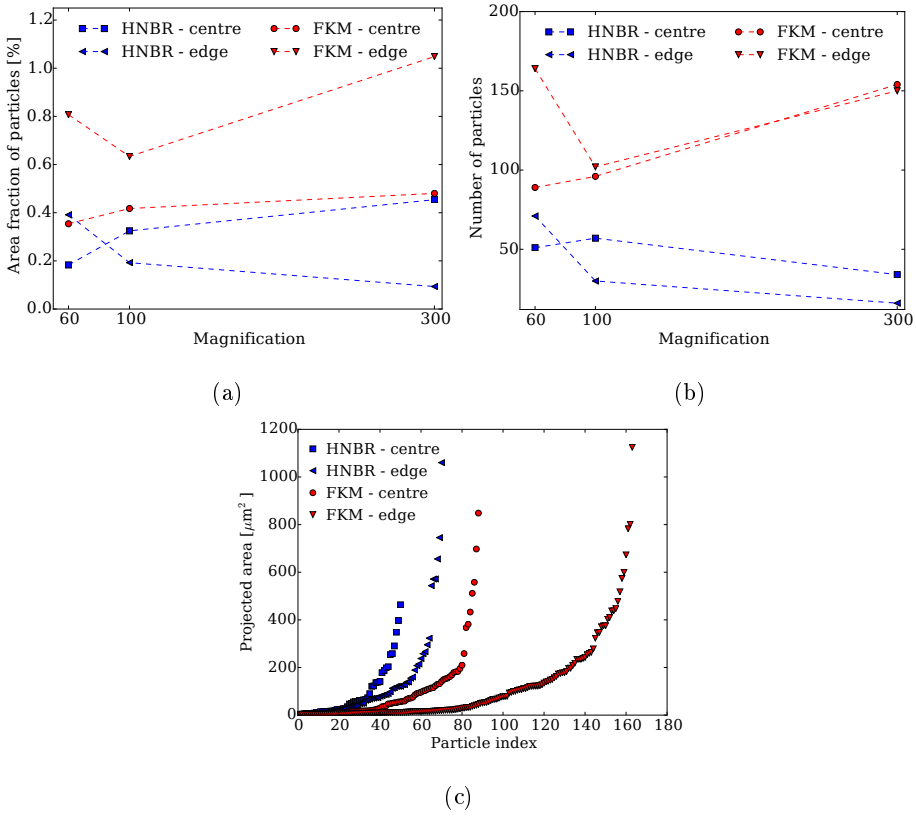

Figure 11: Results obtained from segmentation of the pre-deformation SEM images. (a) Area fraction of particles for all images, (b) the number of particles found in each image, and (c) distribution of particle size for images at 60× magnification, each marker indicates a particle and the x-axis gives the particle index when sorted from small to large.

particles giving rise to a highly triaxial stress situation in the observed area.

While a number of clearly debonding particles could be identified in the in situ images of the HNBR material, only one occurrence of clear matrix cavitation, the one shown at location 2 in Figure 12c, could be observed. It is not known what caused this free cavity to nucleate, but one hypothesis is that it initiated at a location where a particle had fallen out of the surface during production of the rubber mats from which the specimens were cut. This suggests that the debonding mechanism, and not matrix cavitation, is dominating the volume growth of the material in tension. However, it is noted that matrix cavitation could be more pronounced in the interior of the material, where the absence of a free surface would lead to significantly larger local hydrostatic stresses. In general, all debonding particles shown in Figure 12 have a relatively large projected area compared with the majority of the particles indicated in Figure 11c.

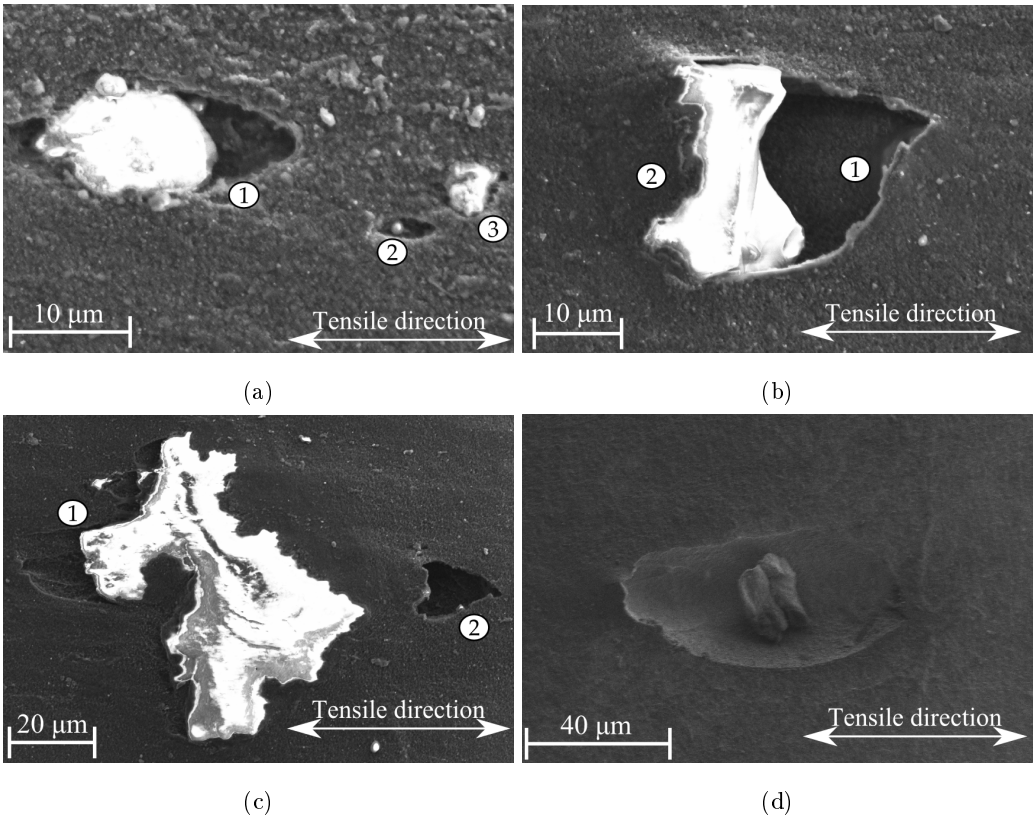

Figure 12: Debonding observed at a nominal longitudinal stretch of approximately 2. (a) Two sided debonding in HNBR, (b) one sided debonding in HNBR, (c) one sided debonding and matrix cavitation in HNBR, and (d) debonding/cavitation in FKM.

5. Numerical single-particle study

5.1. Model

A micromechanical numerical model was used to investigate if the matrix-particle debonding mechanism observed by in situ SEM in Section 4 can explain the volumetric response found in the experimental data of Section 2. It was shown by Willams et al. [46] that such a model would only provide a quantitative prediction of the macroscopic behaviour if a full 3D model was used, taking particle shape, size, distribution, and cohesive strength into account. This would require extensive data on the actual particle distribution, for example through X-ray tomography studies [47, 48], and comprehensive knowledge of the matrix-particle interface behaviour. In addition, running such a model would require considerable computational resources. The purpose here, however, is to do a qualitative study aimed at investigating the mechanisms of matrix-particle debonding, and how this feature affects the macroscopic response. For this purpose, a simple and efficient numerical model could still yield valuable insight [49]. Thus, a cylinder of matrix material containing one spherical particle embedded at its centre is studied. It is important to note that such a model neglects multiple features of the actual materials like the different particle geometries, the size distribution of the particles, the difference in cohesive behaviour for the particles, interaction effects between

the particles and so on.

To incorporate the single-particle model in a finite element framework, the commercial software Abaqus/Standard [50] was used. An illustration of the model and the behaviour in the two loading modes are presented in Figure 13, which also shows the finite element discretization. Approximately 1000 elements were used for the matrix material, while about 200 elements were used to mesh the particle. Four-node axisymmetric elements with reduced integration and hourglass control, named CAX4R in Abaqus, were applied in the analyses. The external boundaries of the model were constrained to remain straight throughout the deformation. The model was exposed to UT loading by applying the stress - time data obtained in the experimental tests to the upper boundary as a negative pressure force, while the vertical external boundary was free to move horizontally. The CAC experiment was modelled by applying the stress - time data measured in the fifth cycle of the corresponding test to the upper surface, while a fixed analytically rigid wall constrained the cell from expanding horizontally. To model the debonding between the particle and the matrix, a cohesive zone was added as an interaction property. The introduction of the cohesive zone also calls for a length scale to be defined in the model and the matrix cylinder was given a height and diameter of 20 micrometres.

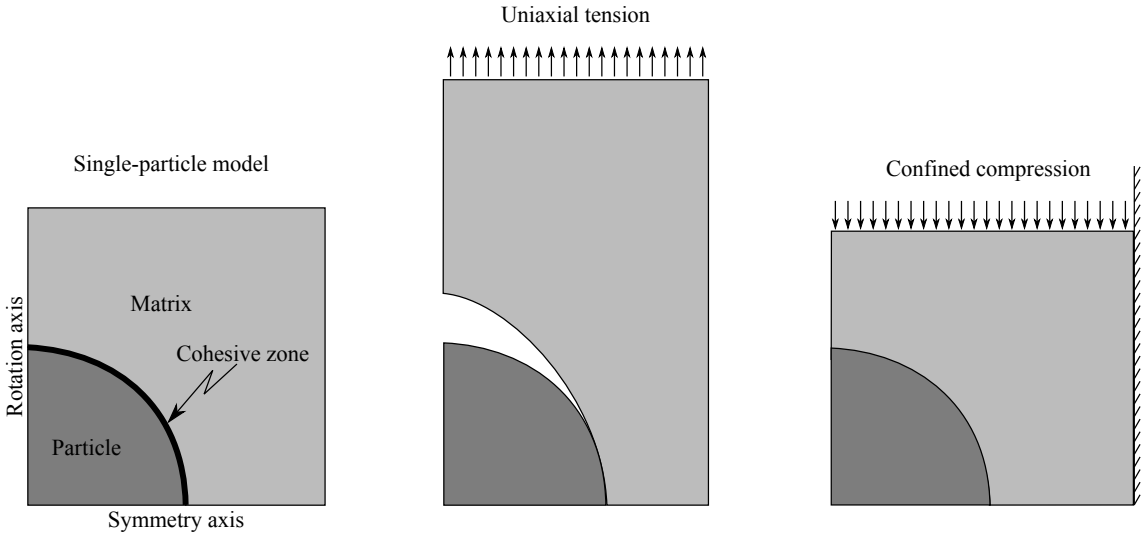

Figure 13: Illustration of axisymmetric single-particle model and its response in the two loading modes, $f_0 = 5$ %.

5.2. Particle size

The macroscopic volume increase obtained in the single-particle model during UT deformation is strongly dependent on the size of the embedded particle, as shown in Figure 14 where the volume ratio obtained at a longitudinal logarithmic strain of 0.7 for simulations with different particle volume fractions is illustrated (for these simulations, no cohesive zone was defined). Comparing with the area fraction of particles in the surface found from the SEM study in Figure 11a (<1 %), it is clear that the volume ratio of particles must be overestimated to get a significant volume

growth. There can be multiple explanations for this fact. First, as already mentioned, the model is too simple to provide quantitatively precise results due to the lack of matrix cavitation, neglecting the particle size distribution, inaccurate modelling of the complex particle geometries, and the lack of particle interaction effects. The latter is assumed the most important effect for the total volume growth, as the interaction between particles leads to increased local hydrostatic stresses, promoting decohesion and volume growth [51, 52]. Second, the area fraction of particles obtained from the micrographs might underestimate the actual volume fraction of inclusions due to sub-pixel particles and/or an inhomogeneous particle distribution through the thickness of the samples.

For the purpose of the following qualitative study, the particle size of the basis model was adapted to a volume fraction f_0 of 5 %, such that a clear volume increase could be obtained in UT loading.

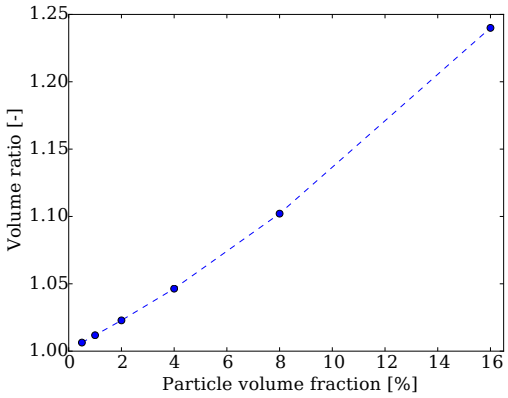

Figure 14: Volume change prediction at a longitudinal logarithmic strain of 0.7 and no cohesion for a set of particle volume fractions.

5.3. Constitutive modelling

For the constitutive modelling of the matrix material, the visco-hyperelastic Bergström-Boyce model implemented in Abaqus, using a nearly isochoric Arruda-Boyce strain energy potential, was applied. The parameters for the model are listed in Table 2 where the same notation as in Abaqus Theory Guide [53] is adopted, with μ being the shear modulus of the spring in the elastic part, λ_m the locking stretch, D the compressibility parameter (related to the bulk modulus by $\kappa = 2/D$), S the scaling of the stiffness between the elastic and the viscous parts, A a scaling parameter for the viscous deformation, c an exponent for the strain dependence of the viscous deformation, and m an exponent for the stress dependence of the viscous deformation. The parameters were chosen such that the experimentally obtained macroscopic stress - strain data in Section 2.1.2 and 2.2.2 were captured in an approximate manner. The embedded filler particle was modelled as linear elastic with Young's modulus of 140 GPa and Poisson's ratio of 0.3, being approximate values for bulk ZnO [54].

μ [MPa]	λ_m [-]	D [1/GPa]	S [-]	A [MPa^{-m}s^{-1}]	c [-]	m [-]
2.5	1.6	1.15	12	0.001	0	6

Table 2: Constitutive parameters used for matrix material in single-particle model simulations.

5.4. Cohesive behaviour

The cohesive zone between the matrix and the particle was modelled as an interaction property using a linear traction-separation law with a quadratic stress criterion. Such a modelling of the cohesive zone has been used in a range of studies, e.g. [30, 55, 56] to name a few. The model is illustrated in the sketch of Figure 15. The stress needed to separate the two surfaces increases linearly with a stiffness k until an initiation stress T_{ini} is reached (coinciding with the initiation deformation δ_{ini}). The load bearing capacity of the cohesive zone is then reduced linearly until a total fracture energy of G_c is reached (taking place at a critical deformation of δ_{crit}). Due to the absolute lack of experimental data on the matrix-particle interface behaviour of the materials, the parameters of the base model were set to be $T_{ini} = 6$ MPa, $k = 6$ GPa/μm, and $G_c = 15$ J/m^2, as this gave a reasonable representation of the experimental results. The critical stress was set equal in normal and shear directions.

To investigate the dependence on the cohesive parameters, the total fracture energy or the initiation stress was changed in consecutive simulations, keeping the other parameters constant. The hydrostatic stress - volume ratio results obtained from this small parameter study are shown in Figure 16. Reducing the fracture energy reduces the slope of the curve after fracture initiation, see Figure 16a, and leads to an increased maximum volume. Changing the initiation stress, on the other hand, yields a clear effect on the hydrostatic stress level at onset of volume growth, as shown in Figure 16b, while the maximum volume ratio immediately before unloading is hardly affected.

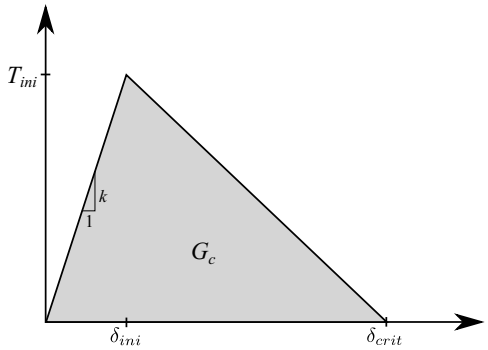

Figure 15: Illustration of the traction-separation law used for the cohesive zone.

It is important to note that the hysteresis loop of the volumetric response in UT, seen in Figure 16, is caused by both viscous effects in the matrix material and the failure of the cohesive zone. This is demonstrated in Figure 17 where the prediction from the base model is compared with the result obtained using a purely hyperelastic matrix material, i.e. the constitutive model is reduced

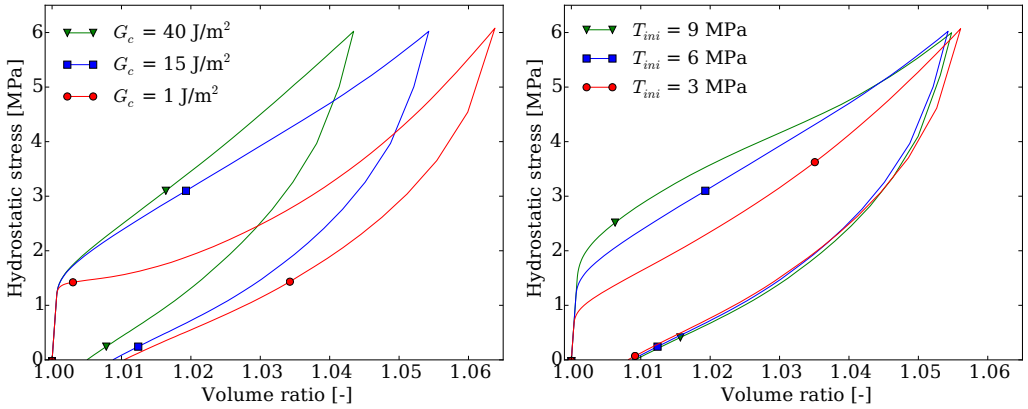

(a) (b)

Figure 16: Parameter study results for the properties of the cohesive zone in the single-particle model subject to tension, (a) dependence on fracture energy and (b) dependence on initiation stress.

to the Arruda-Boyce hyperelastic potential by $S = A = 0$. While a larger total volume increase is seen for the purely hyperelastic model due the more compliant matrix, it is clear that a significant hysteresis loop can be caused solely by the failure of the cohesive zone. It can be noted that removing the viscous effects in the single-particle model would not have any consequence for the CAC response.

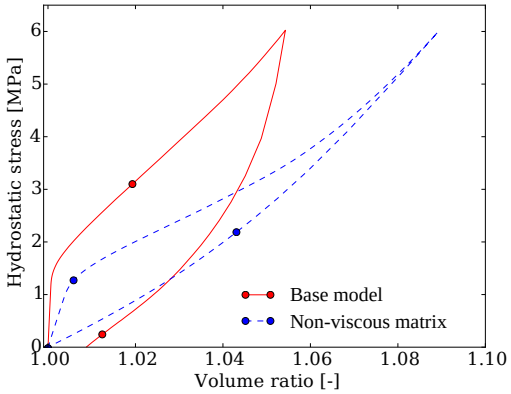

Figure 17: Illustration of the hysteresis loop in tension caused by the cohesive zone.

5.5. HNBR vs FKM behaviour

To get an indication on the source of the difference in UT volumetric behaviour between the HNBR and FKM compounds, two different sets of material parameters, Model A and Model B, were defined to capture the qualitative response of the HNBR and FKM material respectively. From the parametric study in Section 5.4, it was indicated that the difference in volumetric behaviour between the two materials tested in Section 2 can be caused by an increased initiation stress and a reduced fracture energy on average for the cohesive zones in the HNBR compound compared with the FKM, in addition to fewer debonding particles in the HNBR compound leading to less volume

	f_0 [-]	D $[1/GPa]$	T_{ini} $[MPa]$	G_c $[J/m^2]$
Model A	0.018	1.05	30	9
Model B	0.05	1.15	6	15

Table 3: Model parameters used to qualitatively capture the difference between HNBR and FKM behaviour.

growth. The parameters of Model B were set equal to the base model parameters of Section 5.4, while the value of f_0, D, T_{ini}, and G_c were changed for Model A with the following reasoning; f_0 was reduced to get a lower total volume increase in UT, D was reduced to get a slightly stiffer CAC behaviour, T_{ini} was increased to conform with the large stress level at onset of volume growth, while G_c was reduced to get a more compliant volume behaviour after matrix-particle decohesion. The values of the final parameters are listed in Table 3.

The volumetric behaviour in UT deformation of the single-particle models is shown in Figure 18a, while the hydrostatic stress - volume ratio obtained in the CAC simulations can be seen in Figure 18b. The initial volumetric stiffness of the model is related to the bulk modulus of the matrix and particle material for both loading modes and is therefore nearly equal in all simulations. Both loading modes exhibit a good qualitative resemblance of the experimentally obtained results, showing a compliant and viscous behaviour in UT after a critical stress level is reached, while a stiff and purely elastic behaviour was obtained for the volumetric response in the confined axial compression simulations. This shows that the matrix-particle decohesion and cavitation effects found in the in situ SEM experiments can be the explaining mechanisms for the loading mode dependent volume behaviour observed in the macroscopic tests. In addition, the qualitative difference between Model A and Model B is in good correspondence with the difference obtained comparing the HNBR and FKM compounds in the macroscopic tests of Section 2. This gives an indication that the variation in the observed behaviour between the two materials stems from different adhesion properties between the matrix material and the ZnO filler particles for the two compounds. However, as important features like particle interaction effects and size distributions are neglected in the simple model, further studies using more complex modelling procedures should be carried out before definitive conclusions regarding the HNBR and FKM difference can be drawn.

6. Summary and concluding remarks

In this study, HNBR and FKM compounds were tested experimentally in both uniaxial tension and confined axial compression. For the uniaxial tension tests, optical measurements were used to obtain the complete deformation field and thereby capturing the volume change. A moderate volume increase of 5 % was found for the HNBR material, while the FKM compound experienced a large volume change, with an increase of the volume by nearly 20 % for a hydrostatic stress of 6 MPa. In the confined axial compression tests however, very similar results were found between HNBR and FKM compounds, with about 6-7 % reduction of volume for a hydrostatic stress of

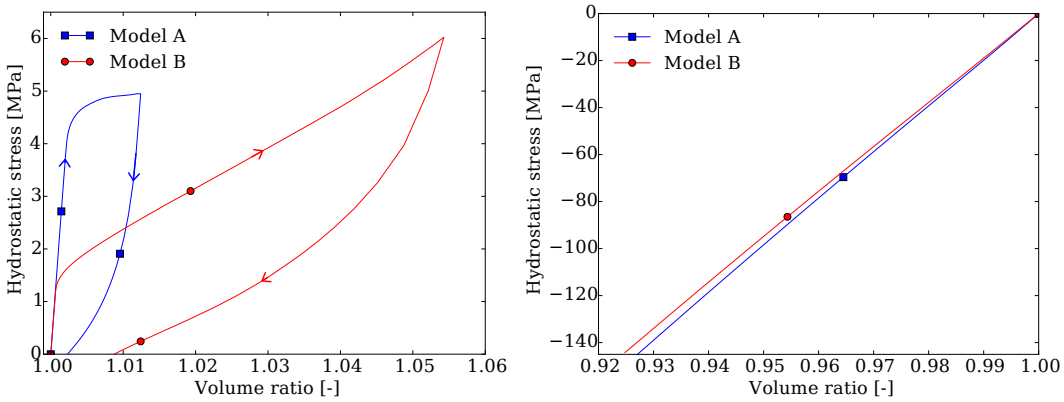

Figure 18: Results from single-particle model simulations in (a) UT and (b) CAC, where Model A and B qualitatively represent HNBR and FKM, respectively.

140 MPa. Comparing the results from the two loading modes, a large difference in the hydrostatic stress - volume ratio behaviour was observed. It was shown that this difference is not captured by available constitutive models for elastomeric materials. The mechanisms responsible for the volumetric behaviour are therefore studied further as a preparation for new micromechanically based constitutive modelling approaches.

To investigate the origin of the volume increase observed in uniaxial tension, an in situ SEM study was performed. Both materials were found to consist of a significant number of ZnO particles, which were shown to debond from the matrix material during tension, causing macroscopic volume growth. In addition, matrix cavitation was observed at the surface.

Based on the SEM experiments, the large difference in volumetric behaviour obtained between the two loading modes was studied by finite element simulations of an axisymmetric single-particle model. The simulations indicated that the volumetric response obtained in the experiments could be qualitatively explained by the interaction between matrix material and filler particles, with decohesion occurring during uniaxial tension. In addition, by changing the parameters of the cohesive zone, the qualitative difference between the HNBR and the FKM material could be described. However, further studies on the effect of particle geometry, size distribution, and interaction effects should be carried out before definitive conclusions can be drawn.

The findings of this study prepare for development of new constitutive models aimed at predicting the volumetric response of particle-filled elastomers exposed to various loading modes. Such models should incorporate the underlying physical mechanism of matrix-particle decohesion such that a viscous and compliant volume growth would be predicted during tension while a stiff and elastic volume response would be obtained during compression.

Acknowledgements

The authors would like to acknowledge Aker Solutions AS for their funding of this research, the suppliers for providing test samples free of charge, Mr Trond Auestad for his assistance with the macroscopic experiments, and Mr Christian Oen Paulsen for his assistance during the SEM study.

References

[1] J. S. Bergström, M. C. Boyce, Constitutive modeling of the large strain time-dependent behavior of elastomers, Journal of the Mechanics and Physics of Solids 46 (1998) 931–954.

[2] C. Miehe, S. Göktepe, A micromacro approach to rubber-like materials. Part II: The micro-sphere model of finite rubber viscoelasticity, Journal of the Mechanics and Physics of Solids 53 (2005) 2231–2258.

[3] G. Ayoub, F. Zaïri, M. Naït-Abdelaziz, J. Gloaguen, G. Kridli, A visco-hyperelastic damage model for cyclic stress-softening, hysteresis and permanent set in rubber using the network alteration theory, International Journal of Plasticity 54 (2014) 19–33.

[4] A. Ilseng, B. H. Skallerud, A. H. Clausen, Tension behaviour of HNBR and FKM elastomers for a wide range of temperatures, Polymer Testing 49 (2016) 128–136.

[5] A. Ilseng, B. H. Skallerud, A. H. Clausen, Volumetric compression of HNBR and FKM elastomers, Constitutive Models for Rubber IX - Proceedings of the 9th European Conference on Constitutive Models for Rubbers, 2015, pp. 235–241.

[6] L. R. G. Treloar, The elasticity of a network of long-chain molecules-II, Transactions of the Faraday Society 39 (1943) 241–246.

[7] M. Mooney, A theory of large elastic deformation, Journal of Applied Physics 11 (1940) 582–592.

[8] R. S. Rivlin, Large Elastic Deformations of Isotropic Materials. IV. Further Developments of the General Theory, Philosophical Transactions of the Royal Society A: Mathematical, Physical and Engineering Sciences 241 (1948) 379–397.

[9] A. Ciesielski, An Introduction to Rubber Technology, Smithers Rapra Technology, 1999.

[10] A. N. Gent, B. Park, Failure processes in elastomers at or near a rigid spherical inclusion, Journal of Materials Science 19 (1984) 1947–1956.

[11] K. Cho, A. N. Gent, P. S. Lam, Internal fracture in an elastomer containing a rigid inclusion, Journal of Materials Science 22 (1987) 2899–2905.

[12] A. Gent, P. Lindley, Internal Rupture of Bonded Rubber Cylinders in Tension, Proceedings of the Royal Society A: Mathematical, Physical and Engineering Sciences 249 (1959) 195–205.

[13] A. Dorfmann, Stress softening of elastomers in hydrostatic tension, Acta Mechanica 165 (2003) 117–137.

[14] E. Bayraktar, N. Isac, K. Bessri, C. Bathias, Damage mechanisms in natural (NR) and synthetic rubber (SBR): Nucleation, growth and instability of the cavitation, Fatigue and Fracture of Engineering Materials and Structures 31 (2008) 184–196.

[15] O. Lopez-Pamies, M. I. Idiart, T. Nakamura, Cavitation in elastomeric solids: I - A defect-growth theory, Journal of the Mechanics and Physics of Solids 59 (2011) 1464–1487.

[16] W. L. Holt, A. T. McPherson, Change of volume of rubber on stretching : effets of time, elongation and temperature, Journal of Research for the National Bureau of Standards 17 (1936) 657–687.

[17] H. Jones, H. Yiengst, Dilatometer Studies of Pigment-Rubber Systems, Rubber Chemistry and Technology 14 (1941) 113–124.

[18] R. Shuttleworth, Volume change measurements in the study of rubber-filler interactions, European Polymer Journal 4 (1968) 31–38.

[19] R. W. Penn, Volume Changes Accompanying the Extension of Rubber, Transactions of The Society of Rheology 14 (1970) 509.

[20] J. B. Le Cam, E. Toussaint, Volume Variation in Stretched Natural Rubber: Competition between Cavitation and Stress-Induced Crystallization, Macromolecules 41 (2008) 7579–7583.

[21] J.-B. Le Cam, E. Toussaint, Cyclic volume changes in rubber, Mechanics of Materials 41 (2009) 898–901.

[22] J. de Crevoisier, G. Besnard, Y. Merckel, H. Zhang, F. Vion-Loisel, J. Caillard, D. Berghezan, C. Creton, J. Diani, M. Brieu, F. Hild, S. Roux, Volume changes in a filled elastomer studied via digital image correlation, Polymer Testing 31 (2012) 663–670.

[23] S. Cantournet, K. Layouni, L. Laiarinandrasana, R. Piques, Experimental investigation and modelling of compressibility induced by damage in carbon black-reinforced natural rubber, Comptes Rendus Mécanique 342 (2014) 299–310.

[24] A. Needleman, Void Growth in an Elastic-Plastic Medium, Journal of Applied Mechanics 39 (1972) 964–970.

[25] V. Tvergaard, Influence of voids on shear band instabilities under plane strain conditions, International Journal of Fracture 17 (1981) 389–407.

[26] J. Faleskog, X. Gao, C. Fong Shih, Cell model for nonlinear fracture analysis - I. Micromechanics calibration, International Journal of Fracture 89 (1998) 355–373.

[27] L. E. B. Dæhli, T. Børvik, O. S. Hopperstad, Influence of loading path on ductile fracture of tensile specimens made from aluminium alloys, International Journal of Solids and Structures 88-89 (2016) 17–34.

[28] A. Steenbrink, E. Van Der Giessen, P. Wu, Void growth in glassy polymers, Journal of the Mechanics and Physics of Solids 45 (1997) 405–437.

[29] L. Cheng, T. Guo, Void interaction and coalescence in polymeric materials, International Journal of Solids and Structures 44 (2007) 1787–1808.

[30] A. S. Ognedal, A. H. Clausen, T. Berstad, T. Seelig, O. S. Hopperstad, Void nucleation and growth in mineral-filled PVC An experimental and numerical study, International Journal of Solids and Structures 51 (2014) 1494–1506.

[31] J. S. Bergström, M. C. Boyce, Mechanical Behavior of Particle Filled Elastomers, Rubber Chemistry and Technology 72 (1999) 633–656.

[32] ISO, 37:2011 Rubber, vulcanized or thermoplastic - Determination of tensile stress-strain properties, Tech. rep. (2011).

[33] E. Fagerholt, T. Børvik, O. Hopperstad, Measuring discontinuous displacement fields in cracked specimens using digital image correlation with mesh adaptation and crack-path optimization, Optics and Lasers in Engineering 51 (2013) 299–310.

[34] ISO, 815-1:2014 Rubber, vulcanized or thermoplastic Determination of compression set Part 1: At ambient or elevated temperatures, Tech. rep. (2014).

[35] C. Harris, M. Stephens, A combined corner and edge detector, in: Alvey vision conference, Vol. 15, Manchester, UK, 1988, p. 50.

[36] M. C. Boyce, E. M. Arruda, Constitutive Models of Rubber Elasticity: A Review, Rubber Chemistry and Technology 73 (2000) 504–523.

[37] S. Doll, K. Schweizerhof, On the Development of Volumetric Strain Energy Functions, Journal of Applied Mechanics 67 (1999) 17–21.

[38] J. E. Bischoff, E. M. Arruda, K. Grosh, A new constitutive model for the compressibility of elastomers at finite deformations, Rubber Chemistry and Technology 74 (2001) 541–559.

[39] T. Sussman, K.-J. Bathe, A finite element formulation for nonlinear incompressible elastic and inelastic analysis, Computers and Structures 26 (1987) 357–409.

[40] J. C. Simo, C. Miehe, Associative coupled thermoplasticity at finite strains: Formulation, numerical analysis and implementation, Computer Methods in Applied Mechanics and Engineering 98 (1992) 41–104.

[41] H. Hencky, The Elastic Behavior of Vulcanized Rubber, Rubber Chemistry and Technology 6 (1933) 217–224.

[42] S. Reese, S. Govindjee, A theory of finite viscoelasticity and numerical aspects, International Journal of Solids and Structures 35 (1998) 3455–3482.

[43] M. Karlsen, J. Hjelen, Ø. Grong, G. Rørvik, R. Chiron, U. Schubert, E. Nilsen, SEM/EBSD based in situ studies of deformation induced phase transformations in supermartensitic stainless steels, Materials Science and Technology 24 (2008) 64–72.

[44] S. van der Walt, J. L. Schönberger, J. Nunez-Iglesias, F. Boulogne, J. D. Warner, N. Yager, E. Gouillart, T. Yu, scikit-image: image processing in Python., PeerJ 2 (2014) e453.

[45] N. Otsu, Threshold selection method from gray-level histograms, IEEE Trans Syst Man Cybern SMC-9 (1979) 62–66.

[46] J. J. Williams, J. Segurado, J. LLorca, N. Chawla, Three dimensional (3D) microstructure-based modeling of interfacial decohesion in particle reinforced metal matrix composites, Materials Science and Engineering A 557 (2012) 113–118.

[47] L. Laiarinandrasana, T. F. Morgeneyer, H. Proudhon, C. Regrain, Damage of semicrystalline polyamide 6 assessed by 3D X-ray tomography: From microstructural evolution to constitutive modeling, Journal of Polymer Science, Part B: Polymer Physics 48 (2010) 1516–1525.

[48] H. A. Cayzac, K. Saï, L. Laiarinandrasana, Damage based constitutive relationships in semi-crystalline polymer by using multi-mechanisms model, International Journal of Plasticity 51 (2013) 47–64.

[49] L. Laiarinandrasana, A. Jean, D. Jeulin, S. Forest, Modelling the effects of various contents of fillers on the relaxation rate of elastomers, Materials and Design 33 (2012) 75–82.

[50] Abaqus, 6.13-1, Dassault Systèmes, 2013.

[51] S. Ghosh, Y. Ling, B. Majumdar, R. Kim, Interfacial debonding analysis in multiple fiber reinforced composites, Mechanics of Materials 32 (2000) 561–591.

[52] P. A. Toulemonde, J. Diani, P. Gilormini, N. Desgardin, On the account of a cohesive interface for modeling the behavior until break of highly filled elastomers, Mechanics of Materials 93 (2016) 124–133.

[53] Abaqus Theory Guide 6.13, Dassault Systèmes, 2013.

[54] C. Q. Chen, Y. Shi, Y. S. Zhang, J. Zhu, Y. J. Yan, Size Dependence of Young's Modulus in ZnO Nanowires, Physical Review Letters 96 (2006) 75505.

[55] J. Segurado, J. Llorca, A computational micromechanics study of the effect of interface decohesion on the mechanical behavior of composites, Acta Materialia 53 (2005) 4931–4942.

[56] H. M. Inglis, P. H. Geubelle, K. Matous, H. Tan, Y. Huang, Cohesive modeling of dewetting in particulate composites: micromechanics vs. multiscale finite element analysis, Mechanics of Materials 39 (2007) 580–595.